Unveiling the control of quenched disorder in rare earth nickelates

Sarmistha Das, V. Eswara Phanindra, Sharon S. Philip, and D. S. Rana*
Department of Physics, Indian Institute of Science Education and Research Bhopal, India
(Received 28 March 2017; revised manuscript received 21 September 2017; published 9 October 2017)

The role of quenched disorder, a key control to obtain novel phases and functionalities, has not yet been determined in the complex phase diagram of $RNiO_3$ (R = rare-earth ion) perovskites. Here we present such a study by investigating $(La_{0.5}Eu_{0.5})NiO_3$ (LENO) having large R-site cation disorder. We show that in the presence of quenched disorder, (i) the resistivity drops by a few orders of magnitude across the metal-insulator transition (MIT) but the MIT shows only a subtle decrease, (ii) compressive films are completely metallic while largely tensile films are completely insulating sans a MIT, (iii) orthorhombic distortion promotes sharp MIT, and (iv) a Fermi liquid behavior even as high temperature resistivity exceeds the Mott-Ioffe-Regel limit with a bad metallic state. The low-energy terahertz conductivity dynamics obey Drude and Drude-Smith models for compressive and tensile films, respectively. All these features of disordered LENO, which are not typical of prototype ordered $NdNiO_3$, reveal an extraordinary sensitivity to slight structural perturbations. This study depicts the ease with which a variety of electronic phases can be tuned in disordered nickelates and emphasize the need to incorporate quenched disorder as a key control in the phase diagram of nickelates.

DOI: 10.1103/PhysRevB.96.144411

I. INTRODUCTION

The research on $RNiO_3$ (R = rare-earth) perovskite nickelates exhibiting first-order metal-insulator transition (MIT), complex magnetic order, and other associated exotic properties has recently drawn immense attention both for fundamental interests and promise in emerging oxides electronics [1,2]. Unveiling the exact mechanism of the MIT nickelates is quite challenging due to the competing energy scales of various interactions among electronic, structural, and spin degrees of freedom. The intertwined electron-electron and electron-phonon interactions do not allow the electronic properties to be accounted for by a simple one electron band model [3,4]. Also, a remarkable structural control of various physical properties allows one to tune different ground states, and explore possibilities for practical applications [5]. The size of a rare-earth cation directly controls the MIT temperature (T_{MIT}) where the Ni-O-Ni bond angle plays a crucial role in the determination of electronic bandwidth and magnetic exchange interactions [1,5–8]. The decreasing size of rare-earth ion decreases the Ni-O-Ni bond angle which further decreases the overlapping of O $2p$ and Ni $3d$ bands, thus, increasing the T_{MIT}. Also, the mismatch between the R-O and Ni-O bond usually stabilizes by the tilting of NiO_6 octahedra [9–11]. The epitaxial strain controlled NiO_6 octahedral rotation induces disproportion in Ni-O bond length which governs the T_{MIT} and associated properties. Overall, the control of the crystal volume by varying the size of R, epitaxial strain, and dimensionality are known to yield various ground states which are far different from that exhibited by bulk crystals [12–18].

A-site cation disorder, also called quenched disorder, is a key parameter which has remarkable control over physical properties of various ABO_3 type complex perovskite oxides. Here, having two or more different size cations at A site, create internal stress which can be released in the lattice through local structure refinement by means of local tilting, rotation, and distortion of BO_6 octahedra, and displacements of oxygen ions from their original initial position [19–22]. The quenched disorder may bring in the possibility of several exotic phases and alter the physical properties in ways which are different by changing the A-site size [23–25]. The quenched disorder has long been extensively studied in perovskite manganites [19,21,23–25]. It is known to induce complex competition among lattice, charge, spin, and orbitals in such a way that the entire phase diagram can be reformed encompassing various new phases with possibilities of practical applications. The role of cation disorder is significant and has been extensive studied in high temperature superconductors and ferrites too [26–28]. In rare earth $RNiO_3$ nickelates, however, the potential of quenched disorder in reconstruction of phase diagram has not yet been explored. To accomplish this, we chose $(La_{0.5}Eu_{0.5})NiO_3$ (LENO) compound which is the mixture of two reasonably extreme members, namely, metallic $LaNiO_3$ (LNO) which does not exhibit MIT and $EuNiO_3$ (ENO) which exhibits MIT at very high temperature ~450 K. Here different size cations La (1.216 Å) and Eu (1.120 Å) generate a large cation size mismatch/quenched disorder at A site. The mixture of these two, i.e., the $(La_{0.5}Eu_{0.5})NiO_3$ (LENO), can be compared with well-studied $NdNiO_3$ (NNO) as the average A-cation radius ($\langle r_A \rangle = 1.168$ Å for LENO) of both these compounds is the same.

The pseudocubic lattice constant of LENO is calculated and found to be similar to that of $NdNiO_3$. Therefore, any disparity among their physical properties can be a consequence of quenched disorder. It may be noted that LNO shows a metallic nature, lacks magnetic order, and possesses undistorted NiO_6 octahedra in the entire temperature range, whereas the ENO exhibit T_{IM} above 400 K with highly distorted NiO_6 octahedra [29–34]. The mixture of these two nickelates, i.e., LENO, shows no characteristic similar to that of LNO or ENO. On the other side, it behaves completely different when compared with the similar average cation size system $NdNiO_3$. The LENO has very large quenched disorder but $NdNiO_3$ has none. It is quantified by calculating the A-site cation size variance which is $\sigma_v^2 = \langle r_A^2 \rangle - \langle r_A \rangle^2 = 0.0023$ Å^2 for

*dsrana@iiserb.ac.in

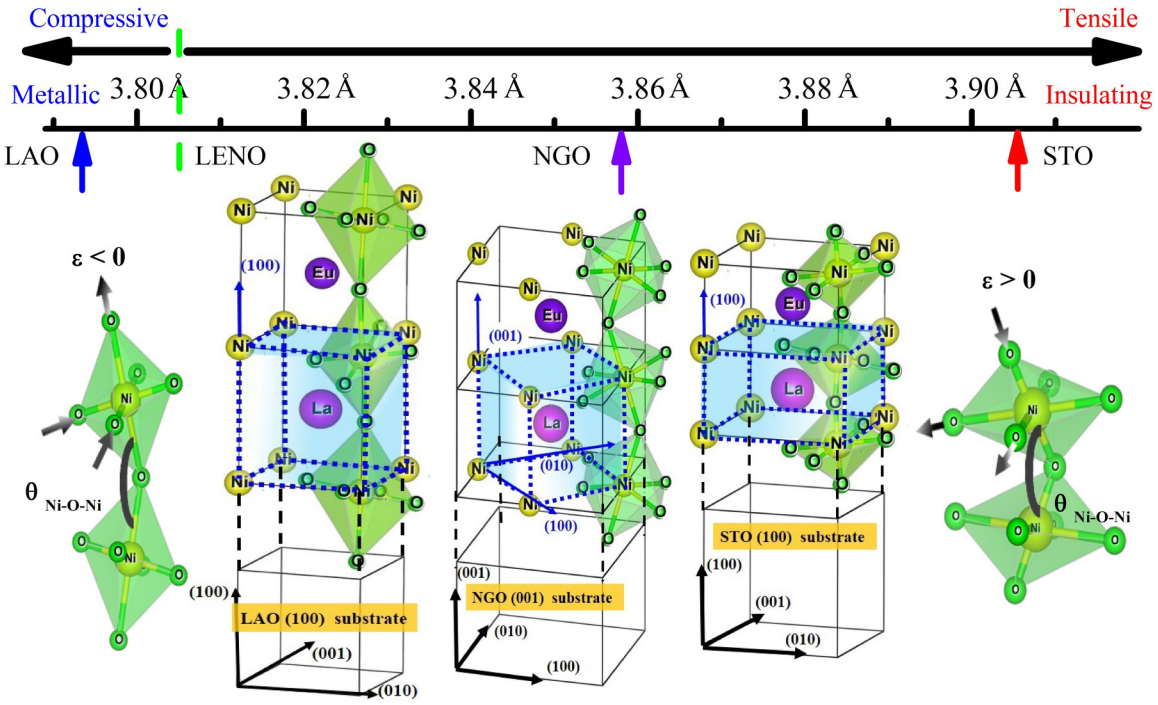

FIG. 1. Schematic representation of structural growth of LENO thin films on LAO (100), NGO (001), and STO (100) substrates with illustration of epitaxial strain (ε) induced octahedral tilting geometry and change in Ni-O-Ni bond angle ($\theta_{\text{Ni-O-Ni}}$) with compressive ($\varepsilon < 0$) and tensile strain ($\varepsilon > 0$).

LENO. Hence, study and comparison of the properties of these two compounds, i.e., LENO and $NdNiO_3$, provides the most suitable platform to elucidate the effect of quenched disorder. In this article we report our studies on tensile and compressive epitaxial thin films of LENO and investigate their structural, electrical, Hall conductivity, and terahertz time-domain spectroscopic properties for understanding the effect of quenched disorder in rare-earth nickelates.

II. EXPERIMENT

The polycrystalline bulk of $La_{0.5}Eu_{0.5}NiO_3$ (LENO) and $NdNiO_3$ (NNO) were prepared using solid state reaction method. Using Vegard's rule for solid state solution, the pseudocubic lattice parameter (a_p) of bulk LENO is determined; the value of a_p is calculated following the relation $\rightarrow a_p\,(\text{LENO}) = [a_p(\text{LaNiO}_3) + a_p(\text{EuNiO}_3)]/2$. The value of a_p for $LaNiO_3$ and $EuNiO_3$ are 3.860 and 3.746 Å, respectively. Hence, the bulk LENO have $a_p \sim 3.803$ Å which is very similar with that of $NdNiO_3$. This polycrystalline bulk sample is used as a target for pulsed laser deposition (PLD) of epitaxial thin films. For LENO and NNO, we choose three different single crystal substrates which induce different type of epitaxial strain and structural symmetries. The LENO and NNO thin films are deposited with compressive strain on cubic $LaAlO_3$ (LAO) (100) substrate, with large tensile strain on cubic $SrTiO_3$ (STO) (100) and with small tensile on orthorhombic $NdGaO_3$ (NGO) (001). Films with three different thicknesses ~12, 30, and 50 nm are deposited on all three substrates. The deposition conditions were: substrate temperature 710 °C, O_2 partial pressure 20 Pa, and laser energy density 1.8−2 J/cm^2. Post-deposition, the films were annealed for 5 min at the O_2 pressure of 200 Pa. The phase purity and epitaxial strain determination were made using x-ray diffraction (XRD) technique on a PanAlytical x-ray diffractometer (Empyrean) equipped with a four-axis cradle. Electrical transport properties, i.e., dc electrical resistivity with four-probe technique and ac Hall effect using Vander Pauw geometry, were studied carried out on a Quantum Design made Physical Property Measurement System (PPMS). The terahertz (THz) time domain spectroscopic (TDS) properties were investigated with the help of a photoconductive (LT-GaAs) antenna-based TERA K-8 spectrometer (Menlo Systems GmbH). The spectrometer is equipped with a closed cycle refrigerator having a temperature variation in the range of 5–320 K. In order to circumvent any possibility of phase error, a reliable process of THz measurement was adopted, as follows. First, a substrate of known thickness is processed in the same conditions of temperature and pressure as optimized for synthesis of thin film in the PLD chamber. Then, THz spectroscopy is performed on this substrate with a variation of temperature from 5 to 300 K. Thereafter, that same substrate was used for thin film fabrication, followed by the THz spectroscopy measurements on the same film.

III. RESULTS AND DISCUSSIONS

A. Structure

In the $RNiO_3$ family, the epitaxial strain modulated electrical properties are governed by the rearrangement of the NiO_6 octahedral structure. The lattice mismatch (ε) plays an important role in controlling the Ni-O-Ni bond angle which evolves into a variation of the NiO_6 octahedra tilting [1,5,9]. A schematic representation (Fig. 1) of the NiO_6

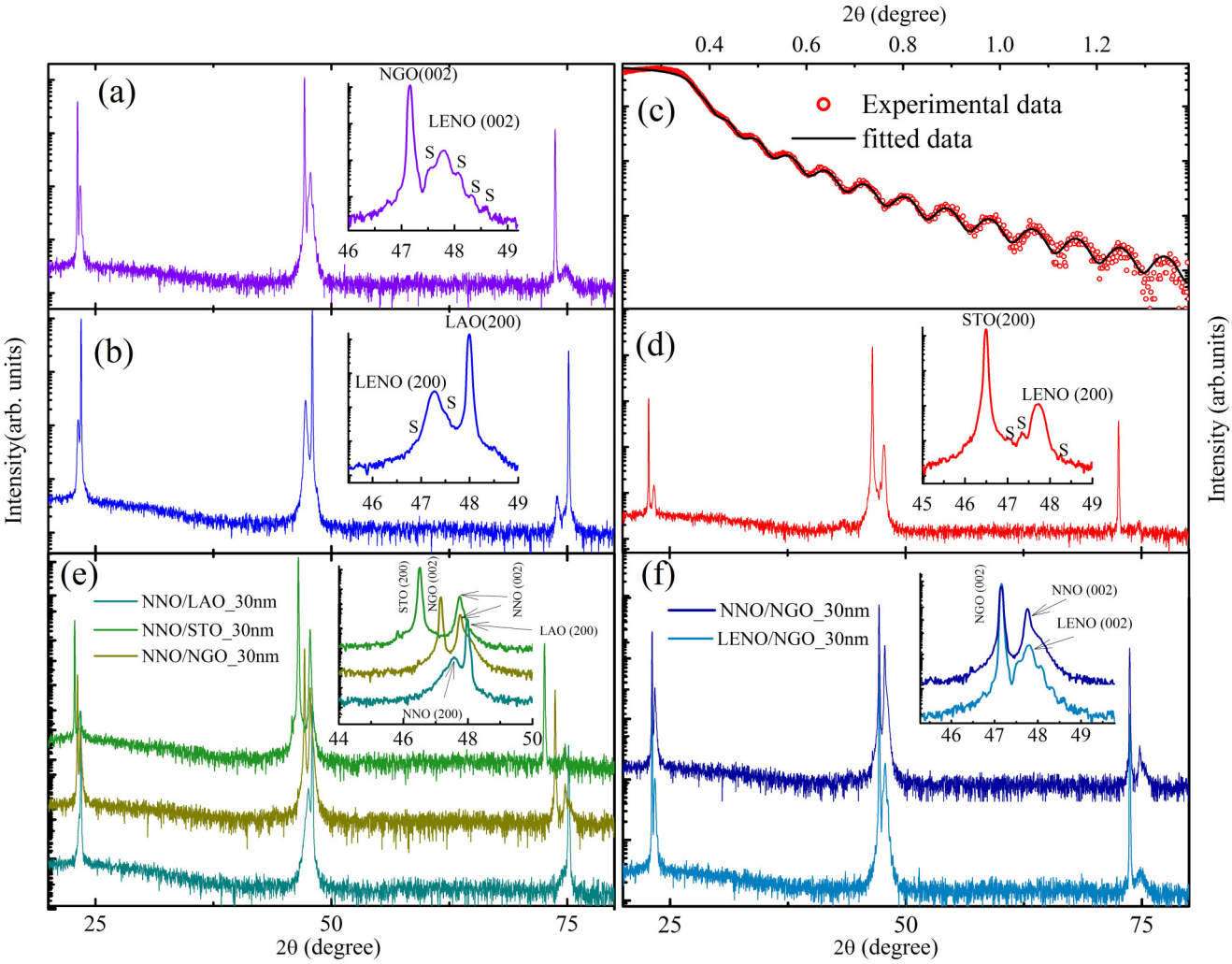

FIG. 2. X-ray diffraction patterns of θ-2θ scans for LENO thin films grown under different strains (a) on NGO (001), (b) on LAO (100), and (d) on STO (100). The corresponding inset contains the magnified symmetric XRD θ-2θ scans around (200) peak. The S signifies the observed satellite peaks of the corresponding films along (200) orientation. (c) X-ray reflectivity profile of LENO film on STO (100), indicating high crystallinity of these samples. The solid black line depicts the best fit of the XRR profile. (e) X-ray diffraction patterns of θ-2θ scans for 30 nm NNO thin films grown on NGO (001), LAO (100), and STO (100). Inset shows the magnified NNO (200) and NNO (002) peaks. (f) The comparative x-ray θ-2θ scans of 30 nm LENO and NNO films on NGO (001) substrate. Inset shows the magnified LENO (002) peak, implying identical lattice parameter.

octahedra tilting in LENO is demonstrated with the variation of the three different substrates. This ε follows the relations between the pseudocubic lattice parameter (a_p) of film (a_f) and substrate (a_s) which can be expressed by $\varepsilon = \frac{a_s - a_f}{a_s} * 100\%$. The calculated values of ε for LAO, NGO, and STO substrates are -0.23%, 1.4%, and 2.6%, respectively. A rough estimation of bond angle for 30 nm LENO film on NGO substrate is estimated as 158.12° which lie in intermediate range values of LNO (165.2°) and ENO (149.7°) [35,36]. The bond angles for 30 nm LENO film on LAO and STO substrates are 162.87° and 154.46°, respectively [12,35,36]. The variation of bond angle with variation of strain is well consistent with each other. These angles are also consistent with the resistivity data, as follows. The compressive film (LENO/LAO) with larger value of bond angle (162.87°) exhibits metallic behavior throughout the entire temperature range. As the bond angle decreases from 158.12° for LENO/NGO to 154.46° for LENO/STO, the insulator-metal transition sets in and then strengthens. The XRD patterns of 30 nm LENO and NNO samples on different substrates, as shown in Fig. 2, suggest all the films to be pure phase with multiple ripples around the main peak. These ripple peaks arise from the multiple reflections from the sharp substrate and film interfaces are known as satellite reflections (S). In addition, the x-ray reflectivity (XRR) measurements [Fig. 2(c)] show the sharp periodic fringes. All these data suggest high quality of LENO thin films. Using the XRR data, the thickness of the samples is estimated to be ~30 nm with surface roughness below 0.4 nm. Figure 2(f) shows that the 30 nm LENO and NNO films have the identical peak positions which further confirm that both the samples have identical lattice constant and exactly similar strained state. In a similar fashion, the XRD patterns of all LENO and corresponding NNO films with the same thickness and the same substrate were compared and found to be matched with each other in a

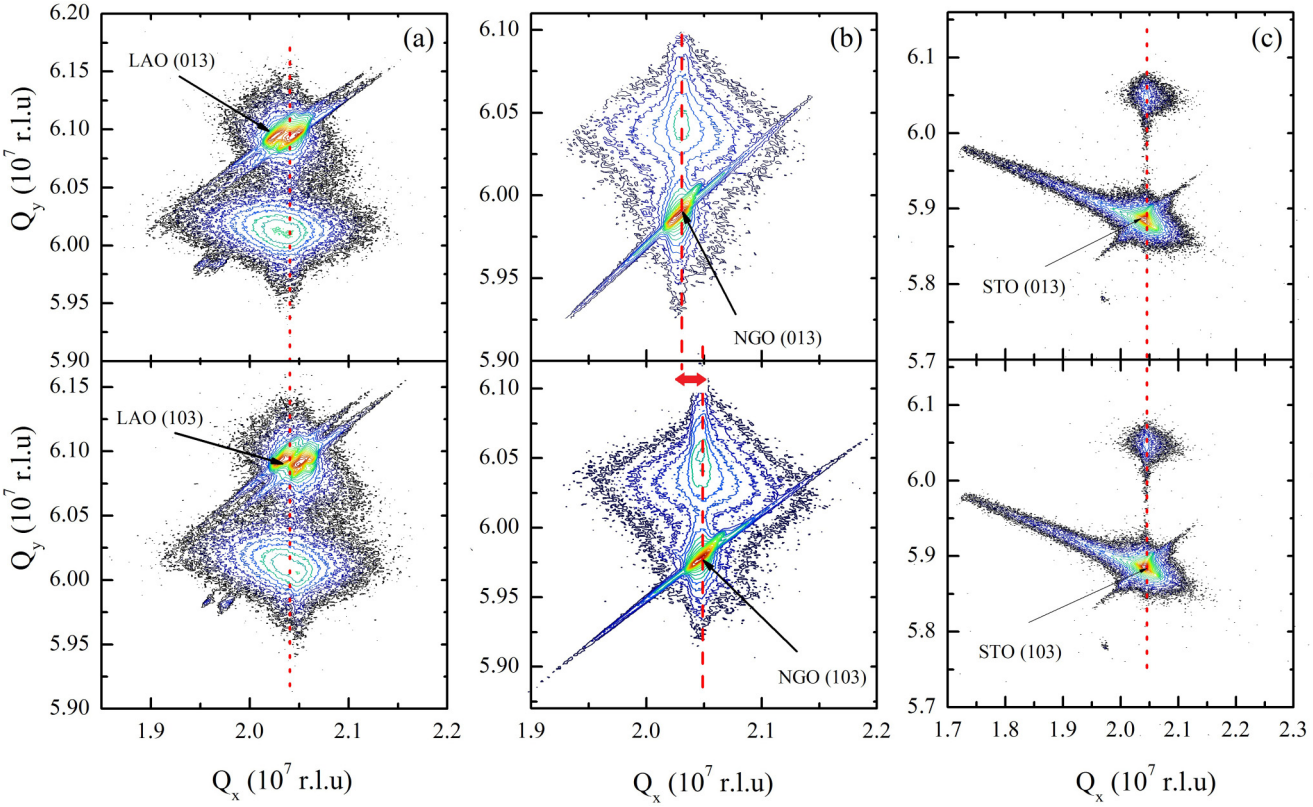

FIG. 3. Reciprocal space mapping studies around the asymmetric 013 and 103 peak of Bragg reflection for pseudocubic diffraction condition of LENO films on (a) LAO (100), (b) NGO (001), and (c) STO (100). The double faced red arrow depicts the dissimilarity in between two different in-plane lattices of orthorhombic symmetry.

similar way as shown for the 30 nm film in Fig. 2(f) (Fig. S1 in Ref. [37]).

The NGO (001) substrate induces orthorhombic distortion and tensile strain while the other two substrates, i.e, LAO (100) and STO (100), induce cubic symmetry in films with compressive and tensile strain, respectively. According to the Poisson effect, the bi-axial strain in thin films stabilizes via modification of all three crystal axes. Hence, the nature of the substrate unit cell structure plays a crucial role in modifying the film lattice parameters. The reciprocal space maps (RSMs) of LENO films with thickness of 30 nm on three substrates are shown in Fig. 3. To confirm the nature of substrate induced unit cell distortion in thin films, the RSM data were collected along two different in-plane axes, namely, (013) and (103) (Fig. 3). All the films are coherently grown as the in-plane film and substrate peaks lie on the same pseudomorphic line. The cubic symmetry induced by the substrates STO and LAO is clearly evident from the RSMs because there is no difference between in-plane film peak positions of (013) to (103) reflections. For the film on NGO, however, the result is entirely different, as for LENO/NGO films, a clear difference among the in-plane film peak positions manifests which follows the corresponding substrate peaks with change of plane direction. As NGO substrate has two different in–plane lattice parameters owing to the orthorhombic symmetry, corresponding different in-plane substrate peaks in RSM data are expected as the in-plane axis changes. This was confirmed from the RSMs of LENO/NGO films suggesting these films to be coherently strained with orthorhombic symmetry. Overall, the RSM data confirm that all the films are coherently strained and that the films on NGO substrate possess orthorhombic symmetry albeit tensile strain. It may be noted that the orthorhombic LENO/NGO films possess a lower symmetric phase other than the tetragonal LENO/LAO and LENO/STO films.

B. Electrical dc resistivity

The temperature (T) dependent resistivity (ρ) data of LENO on different substrates and with different film thicknesses are plotted in Fig. 4. Resistivity of some $NdNiO_3$ films (with no disorder) is also plotted for the scale of comparison with the resistivity of LENO films having large quenched disorder. The compressive LENO/LAO films of all the thicknesses display metallic behavior without any sign of MIT in the entire temperature range of 2–300 K [Fig. 4(a)], while moving from compressive to tensile strained region, the LENO film starts displaying MIT as is seen in the case of tensile and orthorhombic LENO/NGO film [Fig. 4(b)]. With further increase of ε, realized in LENO/STO films, the MIT disappears [Fig. 4(c)]. In this case, the transition from one type of insulating state at high temperature to another type of insulating state occurs at a temperature similar to T_{IM} of LENO/NGO thin films. Such a rich variety of electronic phases suggesting extraordinary sensitivity to epitaxial strain and film thickness is not a property of any other member of the nickelate family. While comparing these features of LENO with well-known NNO, we make some important observations, namely, (i) the compressive NNO films on LAO substrate exhibit MIT

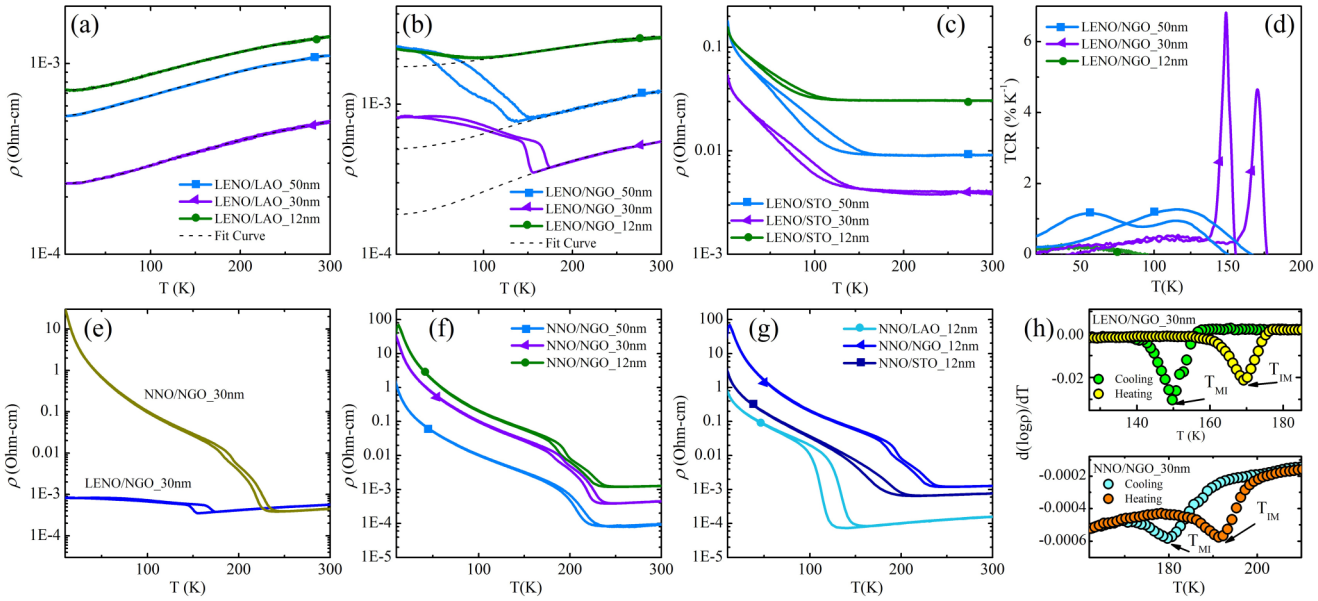

FIG. 4. ρ vs T plot with the fits of Eq. (1) for LENO films on (a) LAO, (b) NGO, and (c) STO. The solid lines are the experimental data and the black dashed lines are the fitted data. (d) The evolution of TCR with temperature and thickness variation for LENO films on NGO. (e) Comparing presentation of ρ vs T data of 30 nm NNO and LENO thin films on NGO substrate. With substrate variation, solid lines are for LENO films and dashed lines are corresponding for NNO films (f) ρ vs T curve with thickness variation of NNO films on NGO. (g) ρ vs T plot for 12 nm NNO films on LAO, NGO, and STO. (h) The T_{MI} and T_{IM} determination from the peaks of $d(\log \rho)/dT$ for 30 nm LENO and NNO thin films on NGO.

at all thicknesses above 8 nm but LENO/LAO films present no signature of MIT and remain entirely metallic down to 2 K for all thicknesses of 12–50 nm [Figs. 4(a) and 4(g)] [37]. (ii) The highly tensile NNO/STO films also exhibit MIT, but LENO (with quenched disorder) do not exhibit any MIT, rather a clear transformation in between two different insulating states is observed [Figs. 4(c) and 4(g)]. (iii) The NNO exhibits a suppression of overall resistivity with increase in film thickness [38,39], while LENO thin films do not follow such thickness dependency. The LENO films clearly follow only one type of trend in resistivity as a function of film thickness; the resistivity decreases as a film thickness decreases, but at very low thicknesses (12 nm is the present case) the trend reverses. This type of resistivity magnitude transition is absent in NNO for which the overall resistivity decreases with increase of thickness down to the thickness of 5 unit cell (∼2 nm) [38,39]. Although the anomaly in resistivity with variation of thickness in NNO can be observed if the thickness goes beyond ∼120 nm [35,40,41], yet a clear understanding of this kind of behavior is lacking. In the next section we will elaborate on this behavior in the LENO system in the light of quenched disorder. (iv) A slight suppression of MIT in LENO (160–180 K) compared to that of NNO (180–230 K). All these marked dissimilarities in LENO and known NNO are an obvious manifestation of quenched disorder which brings in very fine control over the electronic phases.

The nonmonotonical variation of resistivity with film thickness is not unique in the low thickness limit as observed in LENO. In fact in our case, beside the epitaxial strain modulated complex interplay of charge, orbital, and spin, there also exists the cation disorder which is expected to make the ground state much more complicated with respect to a prototype system such as NNO. One plausible reason for such behavior could be oxygen nonstoichiometry in LENO thin films [9,42]. In order to verify this we annealed all the samples in high oxygen pressure ∼500 Pa at 600 °C for 2 h. However, we found that the nonmonotonic behavior of resistivity with thickness continues to persist. Moreover, we did not find any significant change in resistivity. The T_{MI} is unaffected too. These reasons rule out the possibility of oxygen nonstoichiometry in LENO thin films (Fig. S2 in Ref. [37]). Here it may be noted that though the resistivity (say in the metallic region) varies nonmonotonically, the variation is small up to two factors. This is unlike other reported studies in which the variation in resistivity may go beyond one order of magnitude. Such behavior may be understood to arise from a complicated mechanism resulting from the structural changes and dimensionality effect with phase transition. There are two major competing phenomena in LENO as the dimensionality varies: (i) the intrinsic quenched disorder and (ii) the defect center formation as a secondary effect of strain relieve mechanism in lattice. The 12 nm sample is a more strain dominated state because of its low dimensionality. Hence, the 12 nm samples are more prone to defect formation to relieve the strain in the lattice and the defect cluster is randomly distributed in the lattice attributing to high resistive behavior. With a further increase in thickness, i.e., for 30 nm film, the defect formation is minimized with respect to the 12 nm sample. This is because of the larger thickness of 30 nm film and hence a larger volume, a rearrangement of the defect center becomes much easier in the presence of quenched disorder to get energetically stable, thus, resulting in a less resistive behavior. But the rearrangement must have some limit and further increase in thickness, i.e., 50 nm films, the defect clusters may randomly distribute through the lattice, which increase the resistive behavior more than 30 nm film but not large enough to dominate the randomness of 12 nm thin film.

The sharpness of MIT is a key parameter to reflect on the quality of phase transition. To determine the sharpness of transition of LENO/NGO films, the temperature coefficient of resistivity (TCR $= -\frac{1}{\rho}\frac{d\rho}{dT} * 100\%$) was calculated [Fig. 4(d)] [35]. The 30 nm LENO/NGO film exhibits the very sharp TCR peak values with FWHM ∼7−8 K for heating and cooling cycles. As the thickness increases to 50 nm, the TCR peak broadened and also further the peak splits at 50 nm, which is the similar to observation of NNO film on NGO. The most plausible explanation is the electric and magnetic transition decoupling ability of orthorhombic NGO substrate [35]. No proper peak can be observed in the TCR value for LENO sample on STO (data not plotted) but the phase separated hysteresis is clearly present at the low temperature insulating region. This also depicts that the tensile epitaxial strain derived insulating transition is not completed yet. The sharp and well pronounced TCR value for 30 nm LENO films suggest a very high quality of film which is a highly desired attribute for THz spectroscopic studies.

A summary of the comparison of disordered LENO and ordered NNO can be elucidated from Fig. 4(c). A comparison of these two films with thickness 30 nm on NGO substrate shows that their metallic state exhibits the same resistivity but in the insulating state, i.e., below MIT the resistivity differs up to a humungous 4–5 orders in magnitude. Similarly, a comparison of the two across all substrates for 12 nm films clearly shows that all NNO films exhibit MIT on all substrates, whereas the LENO film exhibits MIT only on NGO substrate. A comparison of different thickness films of two compounds on the NGO substrate too points out both qualitative as well as quantitative differences.

1. Bad metallic non-Fermi liquid (NFL) to Fermi liquid (FL) crossover

In general, bad metals are known to violate the Heisenberg's uncertainty principle where they exhibit persistent saturation resistivity (ρ_s) over the Mott-Ioffe-Regel (MIR) limit, which implies the minimum limit of relaxation time/carrier lifetime (τ) to be unphysical. Hence, for the bad metals with relative very low conductivity (σ) than for conventional metal, τ goes beyond the minimum boundary of the MIR limit while exhibiting a metallic nature [9,38]. Nickelates are well known to exhibit bad metallic conductivity. The prototypical NNO exhibits bad metallic behavior with NFL metallic phase upon compressive epitaxial strain [38]. The resistivity data of LENO films were analyzed in this framework. It may be seen that the LENO too exhibits bad metallic behavior. To quantify this, we used a parallel resistor model which includes the resistor term ρ_{sat} acting in parallel with NFL resistor (ρ_{NFL}). Therefore, the total temperature dependent resistivity [$\rho(T)$] follows the relation a $\rho(T) = \frac{\rho_{NFL}\,\rho_S}{\rho_{NFL}+\rho_S}$. Again, ρ_{NFL} can be expressed as $\rho_{NFL}(T) = \rho_r + AT^{\alpha}$, where ρ_r is residual resistivity and coefficient A is a measure of the electron-electron scattering strain. The exponent α defines the boundary between FL and NFL phases; $\alpha \sim 2$ for FL system and ∼1.5 for NFL systems. The temperature dependent ρ can be expressed as [38]

$$\frac{1}{\rho(T)} = \frac{1}{\rho_r + AT^{\alpha}} + \frac{1}{\rho_S}. \quad (1)$$

The metallic part of each LENO sample is fitted with this equation and extended down to a low temperature region and is plotted in Figs. 4(a) and 4(b). The LENO samples were divided into NFL and FL depending on the value of α. The LENO films exhibit FL behavior for both compressive and tensile strained cases and also maintain FL behavior for different thickness films. The value of α lies in the FL zone (∼1.88) for compressive strained fully metallic LENO films on LAO, and for tensile strained LENO/NGO, $\alpha \sim 1.98$, implying again the FL nature of films with the presence of MIT. Mikheev *et al.* have also shown NFL behavior in the metallic state of $LaNiO_3$/LAO films using the same shunt resistor model [Eq. (1)]. Overall, this FL behavior of LENO/LAO film vis-a-vis reported NFL behavior of NNO/LAO and $LaNiO_3$/LAO film suggest that the quenched disorder coupled with strain is the most plausible cause of anomalous behavior in the former.

The MIR limit for LENO films on different substrates was calculated. It has strong correlation with the dimension of the carrier mean free path. As the mean free path becomes comparable with the interatomic spacing (d), the ρ_{MIR} follows the relation $\rho_{MIR} = 3\pi h/2e^2k_F^2d$, where, h is Plank's constant, e is the elementary charge, and k_F is the Fermi wave vector [9,38]. The k_F has nonlinear relation with charge carrier density (n) as $k_F^2 = 3\pi^2 n$, where n is determined from Hall resistivity data and d is derived from XRD data. The d varies for films on different substrates. The calculated values of ρ_{MIR} are 0.3 and 0.2 mΩ cm for LAO and NGO, respectively, and for all thin films the value of ρ_{sat} exceeds this MIR limit, suggesting a bad metallic behavior. For LAO, the $\rho_r < \rho_{MIR}$, while for NGO, the $\rho_r > \rho_{MIR}$. Up to quantum critical limit, all these results are very similar to those of NNO [9,38].

2. Film thickness dependent MIT

The evolution of the MIT hysteresis gives the insight of insulating phase formation and dynamics of phase transition [43]. From the peak value of $-d(\log\rho)/dT$, the values of transition temperatures T_{MI} (cooling protocol) and T_{IM} (heating protocol) were determined for all LENO and NNO films on NGO, as plotted for 30 nm films in Fig. 4(h). The T_{IM} first increases and then decreases as the thickness varies from 12 to 50 nm. This is a quite similar trend as observed in tensile strained NNO/STO [41] and in that case the critical thickness for which the T_{IM} value starts to decrease with an increase in thickness is 18 nm (∼45 unit cell). Compared to this, the LENO/STO films do not exhibit MIT. For LENO/NGO films, the critical thickness is found to be much larger ∼30 nm (∼77 unit cell) [41]. Moreover, the NNO/LAO films also exhibit strong thickness dependence in T_{IM} while in contrary LENO/LAO sans any transition with thickness variation.

C. THz Time-domain spectroscopy of LENO films

Combining high frequency THz dynamic response with the static transport properties is essential to obtain deeper insights about the ground state of the materials. In this context, the 30 nm thick LENO/LAO and LENO/NGO films were probed using THz time domain spectroscopy in transmission mode. With help of Fresnel's equations, the THz complex optical conductivity and dielectric constant are extracted from the complex refractive index data in the range 0.2–1.5 THz. The

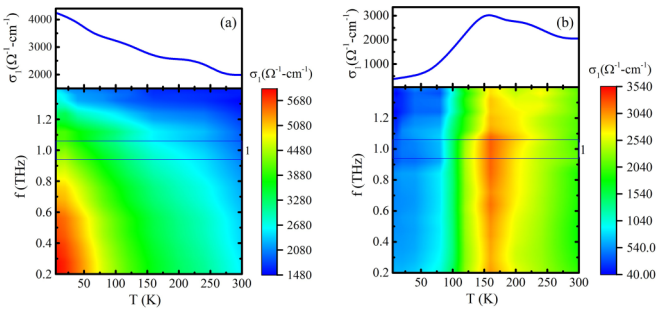

FIG. 5. THz real conductivity σ_1 as a function of THz frequency (f) with variation of temperature (T) along with the σ_1 vs T profile at fixed THz frequency of 1 THz for LENO thin films on (a) LAO and (b) NGO.

real component (σ_1) of complex THz optical conductivity [$\sigma^*(\omega) = \sigma_1 + i\sigma_2$] as a function of THz frequency ($f = \omega/2\pi$) and temperature (T) is plotted as a contour diagram for two different substrates, as shown in Fig. 5. The σ_1 vs T profile for $f = 1$ THz is also shown for LENO/LAO and LENO/NGO films in Fig. 5. For a fixed f, the LENO/LAO is metal in the entire temperature range but the LENO/NGO exhibits MIT at 160 K. These THz conductivity data are consistent with the dc conductivity data. As both thin film samples exhibit different types of frequency dependent THz conductivity data, both real and imaginary components of $\sigma^*(\omega)$ were modeled with various THz conductivity theories, as follows

D. Drude behavior on LENO/LAO film

The σ_1 and σ_2 (imaginary conductivity) components of THz complex conductivity (σ^*) as a function of frequency at different temperatures are plotted in Fig. 6 for LENO/LAO film. A decrease in σ_1 with increasing THz frequency and positive σ_2 point towards Drude behavior at all the temperatures. The total spectral weight decreases with an increase of temperature. All these are well-known features of the metallic system with free carriers. The frequency dependent Drude conductivity model of the free electron system has been employed here to fit the THz response of LENO/LAO film as

$$\sigma^* = \frac{\epsilon_0 \omega_p^2}{\Gamma - i\omega} - i\epsilon_0\omega(\epsilon_\infty - 1), \qquad (2)$$

where ε_0 is free space permittivity, ω_p is plasma frequency, Γ is the scattering rate, and ϵ_∞ is the dielectric constant at high frequency with limit of infinity. The σ_1 and σ_2 were fitted simultaneously with the Drude model (Fig. 6). It is clearly seen that the spectra very well follow the Drude model. For an ideal metal, the $\sigma_1(\omega)$ shows a delta function at $\omega = 2\pi f = 0$ and the peak at $\omega = 0$ broadens due to the carrier disorder in the material. As shown in Fig. 6, the presence of a broad σ_1 peak at $\omega = 0$ indicates the presence of disorder in LENO/LAO film. From the scattering rate Γ and the relaxation time $\tau = 1/\Gamma$, as calculated from the fittings (inset of Fig. 6), it may be seen that τ decreases slightly with an increase in temperature. This suggests the increase in charge carrier scattering rate as the temperature becomes higher and the Drude peak broadens at zero frequency. However, it maintains an overall constant value signifying bad metallicity [9]. Overall, the low energy

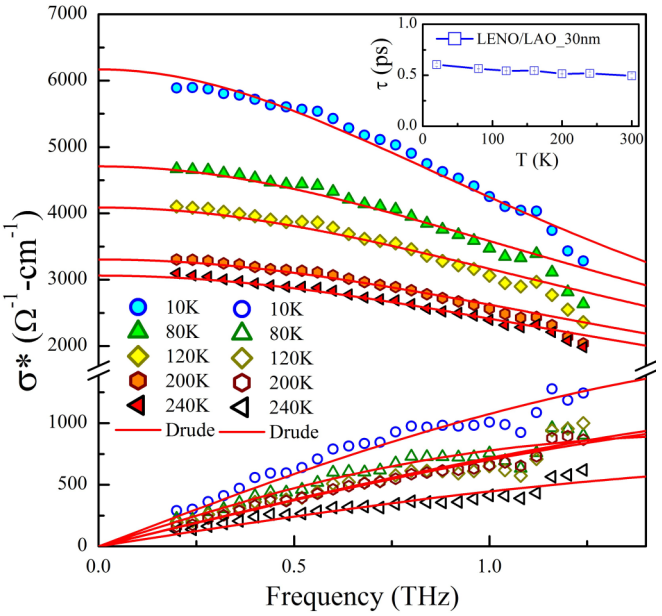

FIG. 6. THz optical responseof LENO thin film on LAO (100) substrate. The THz complex conductivity σ^* vs THz frequency (f) with variation of temperature (T). The filled and blank symbols signify the real (σ_1) and imaginary (σ_2) part of σ^*, respectively. The solid red lines are the fit with Drude model. Inset depicts the temperature dependence of relaxation time (τ) of 30 nm thick LENO thin films on LAO as estimated from the Drude fitting.

dynamics of LENO/LAO film follow a conventional metallic behavior in the entire temperature range.

E. Drude-Smith conductivity dynamics in LENO/NGO film

The THz frequency dependent σ_1 and σ_2 for LENO/NGO film at different temperatures are plotted in Fig. 7. There exists a very clear transition in frequency dependent σ_2 in the vicinity of MIT. Below the transition, σ_2 is positive in magnitude. Above the MIT, the σ_1 starts exhibiting a subtle positive slope simultaneous to the crossover in the sign of σ_2. This response was modeled within the framework of the Drude-Smith (DS) backscattering model, which allows the deviation from the Drude model owing to the presence of disorder in the sample. According to the DS model, σ_1 gets suppressed at the low frequency zone and the spectral weight shifts to the high frequency region. As per the DS model,

$$\sigma^* = \frac{\epsilon_0 \omega_p^2}{\Gamma - i\omega}\left[1 + \sum_n \frac{c_n \Gamma}{\Gamma - i\omega}\right] - i\epsilon_0\omega(\epsilon_\infty - 1). \qquad (3)$$

Here, apart from the Drude term, the second term in square bracket refers to the initial velocity of the carriers retained after encountering a certain number of scattering events. The n refers to the number of collision at the time of scattering and can have a value from 0 to ∞. The coefficient c_n signifies the fraction of carrier's initial velocity retained after the nth collision. One scattering event refers to $n = 1$ and $c_n = c_1 = c$. The value of c ranges from 0 to -1. For $c = 0$, Eq. (2) reduces to the simple Drude model while $c = -1$ refers to full backscattering of carriers for the DS model.

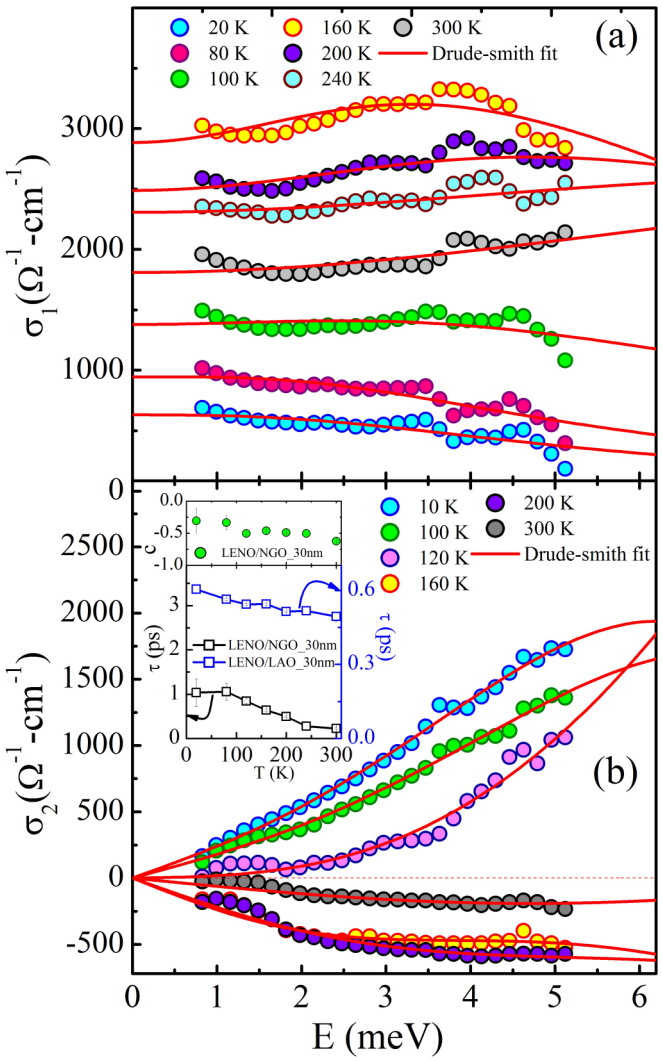

FIG. 7. THz optical response of LENO thin film on NGO (001) substrate. (a) Real (σ_1) and (b) imaginary (σ_2) THz conductivity spectra with variation of THz photon energy (E). The solid red lines are fit with the Drude-Smith model. Inset (b) depicts comparison among the temperature dependence of relaxation time (τ) of 30 nm thick LENO thin films on LAO and NGO substrates. The temperature dependent variation of disorder parameter (c) for 30 nm thick LENO film on NGO is shown in inset (b).

The DS model provides an excellent simultaneous fit for the σ_1 and σ_2 of LENO/NGO film. Figure 7 depicts the fitted data of the complex conductivity. The σ^* vs THz energy (E) plot shows with two significantly separated temperature regions. In the low temperature (5–100 K) region, the σ^* vs E spectra follows the DS model with $c \sim -0.33$. With an increase in temperature, the σ^* gradually follows the DS model with a maximum c of ~ -0.6. From the fits to this model, the value of scattering rate Γ is extracted and relaxation time τ is calculated and plotted in the inset of Fig. 7(b). A trend similar to that of LENO/LAO film can be observed, though a subtle sign of higher scattering rate above the transition region is noticeable. Overall, the carrier scattering event can be divided into two temperature regions, (i) $T < T_{IM}$ and (ii) $T \geqslant T_{IM}$. In the former case, the carriers follow the DS model with nearly constant but low values of τ and $-c \sim 0.3$. But for the latter case, the charge carriers scatter due to the presence of disorder in the system. This type of scattering event is far from being isotropic. The scattering rate also starts increasing just above where the transition occurs while following the DS model. A discernible increase in disorder right above the MIT is apparent as $-c$ increases to 0.6 [inset Fig. 7(b)]. The presence of disorder accounting for DS carrier dynamics is generally attributed to oxygen nonstoichiometry, grain boundaries, and other crystal defects. In the present case, the samples are high quality epitaxially strained single phase films, thus, discarding the possibility of grain boundaries other extrinsic defects are as likely the cause of backscattering. The presence of oxygen vacancies, however, is a likely cause, as it known that the tensile strain makes the perovskite films susceptible to such defects. Another reason could be phase separation arising from the coexistence of insulating and metallic nanosized grains. This is because the increase in value of $-c$ above the MIT cannot be explained by the mere presence of oxygen defects. This needs the presence of dynamic disorder, such as coexistence of two phases above MIT due to incomplete transition [43]. Furthermore, a nonzero and temperature dependent c in tensile and orthorhombic LENO film with highest TCR is a clear signal of quenched disorder present in the system. Such behavior is missing in the films with cubic symmetry. It may also be noted despite substrate induced orthorhombicity in LENO/NGO film, there is no manifestation of a charge-density-wave (CDW) mode in THz conductivity. This is unlike in NNO films [44] which exhibit a clear CDW mode in orthorhombic symmetry.

Overall, this is a study that unveils quenched disorder as a key control parameter in the nickelate phase diagram. In perovskite manganites, in which intense research spanned over two decades, the quenched disorder enriched the phase diagram by intricately altering the balance of energetics of various fundamental interactions, induced several new phases, realized ultrasharp phase transitions, etc. The present study in disorder LENO nickelate promises such potential. The new dc and THz electronic phases of LENO can enrich the phase diagram of nickelates. In the presence of quenched disorder, the complex entanglement of NiO_6 octahedra can create new ground states. This may occur, as known in the case of manganites, by altering local oxygen displacement via tilting NiO_6 octahedra. In the present study, these effects may be visualized by comparison of disordered LENO with ordered NNO, as follows. We introduce the concept of local oxygen displacement due to quenched disorder. We visualize and present a schematic model of cation and anion environment of LNO and ENO (Fig. 8). The LENO system possesses a large nonzero variance ($\sigma_v > 0$) compared to none on NNO. In the latter, the quenched disorder due to different sized cations at A site induces lattice distortion which may stabilize by the shifting local oxygen ion, in addition with tilting NiO_6 octahedra. This may induce a complex entanglement in between average R-cation size induced NiO_6 octahedra tilting and local oxygen displacement. Such effects can be a potential source of all the predominant features of LENO that are missing in ordered NNO. The local oxygen displacement, as suggested above, which plays an active role in the distortion of NiO_6 octahedra, can also be a source of backscattering of

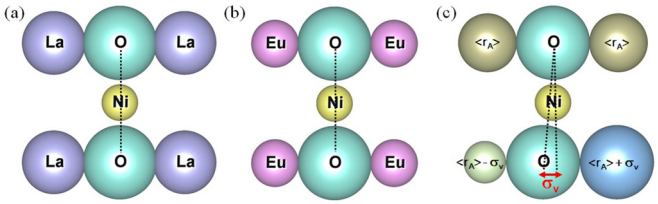

FIG. 8. Schematic representation for the local oxygen displacement in a perovskite system having cation disorder with finite σ_v value. A schematic fragment of ideal cubic structure with $\sigma_v = 0$ for (a) $LaNiO_3$ and (b) $EuNiO_3$ perovskites. In these systems the oxygen and Ni ions are closely packed and there is no possibility to alter the oxygen ion position. (c) The perovskites structure with finite σ_v value and average cation radius $\langle r_A \rangle$ which resemble the $La_{0.5}Eu_{0.5}NiO_3$ structure. In such systems, due to the presence of σ_v, the A-site cation size distribution follows the relation $\sigma_v^2 = \langle r_A^2 \rangle - \langle r_A \rangle^2$ which induces local oxygen displacement in the presence of quenched disorder.

carriers resulting in DS type of THz conductivity in tensile LENO films.

Here it is imperative to invoke the account of a variety of research based on quenched disorder in perovskite manganites. In these systems, intense research spanned over two decades, the quenched disorder enriched the phase diagram by intricately altering the balance of energetics of various fundamental interactions [25,45–48], induced several new phases [45,49], realized ultrasharp phase transitions [50], etc. [51]. A comparison of manganites and nickelates is imperative because of a few quite similar physical phenomena exhibited by these two classes of perovskites. Metal-insulator (MIT) transition, change-order, spin-order, charge-density waves, epitaxial strain induced novel electronic and magnetic phases, etc., are some of the common phenomena that both these class of compounds are identified with and these phenomena are the results of competition of energetics in charge, spin, lattice, and orbital interactions [51]. Major effects of quenched disorder in manganites are reduction in MIT temperature [19], significant reduction in sharpness of MIT [21,22,24], melting of charge-ordered state to a charge-liquid metallic state [23,52], transition from antiferromagnetic to ferromagnetic state, magnetic field dependent successive ultrasharp electronic and magnetic phase transitions, etc. All the effects of cation/quenched disordered manganites can be summed as: (i) in the charge ordered systems, the cation disorder tends to induce the metallic state and (ii) in the manganites with I-M transition, the cation disorder tends to make the transition shallower, reduces sharpness, and enhances the resistivity along with simultaneous reduction in transition temperature. A conjecture of these effects can be clearly made with the present results of nickelates. The observation of lower MIT temperature, shallower transition, complete transformation of MIT state to a metallic state in compressive films and enhanced resistivity, and lack of MIT in tensile films (LENO/STO) seem to clearly agree with the disorder effects of manganite class of compounds. One of the widely accepted reasons for these disorder effects in manganites is the electronic phase separation, implying existence and competitions between fractional volumes of the metallic and insulating phases. While overall effects of cation disorder in nickelates seem to be similar to that of manganites. The existence of phase separation, and its definite interaction with the cation disorder effects in the former, cannot be ascertained yet and need a different framework of experimental investigations.

IV. SUMMARY

To summarize, in order to understand the effect of quenched disorder in $RNiO_3$ nickelates, we made detailed investigations on structural, electrical, and THz low energy carrier dynamics on tensile and compressive strained films of $(La_{0.5}Eu_{0.5})NiO_3$ having large R-site cation-size disorder and compared these properties with those of the ordered $NdNiO_3$, having the same R-site cation size sans any disorder. In this study we showed that disorder modulates the electrical properties to an extent that it induced new phases which can then be easily be tuned with an additional control of strain. A large change in the resistivity, albeit a sharp MIT and a dominant strain induced MIT in both the metallic and insulating regions, manifest as one traverses from compressive to tensile strain, persistence of a Fermi liquid behavior even as high temperature resistivity exceeds the Mott-Ioffe-Regel limit, and a variety of THz carrier dynamics form a unique combination of novel features realized in nickelates. Manifestation of these properties suggests an extraordinary sensitivity of complex phases to slight structural perturbations amid quenched disorder, which further emphasizes the potential as well as the need for extensive explorations on other similar nickelates with varying disorder to incorporate it as a key control in their phase diagram.

ACKNOWLEDGMENTS

D.S.R. thanks the Science and Engineering Research Board (SERB), Department of Science and Technology (DST), New Delhi, for financial support under research Project No. EMR/2016/003598. Financial support from DST-FIST program is also thankfully acknowledged.

[1] J. B. Torrance, P. Lacorre, A. I. Nazzal, E. J. Ansaldo, and C. Niedermayer, Phys. Rev. B **45**, 8209 (1992).

[2] T. Mizokawa, D. I. Khomskii, and G. A. Sawatzky, Phys. Rev. B **61**, 11263 (2000).

[3] S. R. Barman, A. Chainani, and D. D. Sarma, Phys. Rev. B **49**, 8475 (1994).

[4] S. D. Ha, R. Jaramillo, D. M. Silevitch, F. Schoofs, K. Kerman, J. D. Baniecki, and S. Ramanathan, Phys. Rev. B **87**, 125150 (2013).

[5] J. L. Garcia-Munoz, J. Rodriguez-Carvajal, P. Lacorre, and J. B. Torrance, Phys. Rev. B **46**, 4414 (1992).

[6] J.-S. Zhou, J. B. Goodenough, and B. Dabrowski, Phys. Rev. B **67**, 020404 (2003).

[7] I. Vobornik, L. Perfetti, M. Zacchigna, M. Grioni, G. Margaritondo, J. Mesot, M. Medarde, and P. Lacorre, Phys. Rev. B **60**, R8426 (1999).

[8] K. Okazaki, T. Mizokawa, A. Fujimori, E. V. Sampathkumaran, M. J. Martinez-Lope, and J. A. Alonso, Phys. Rev. B **67**, 073101 (2003).

[9] R. Jaramillo, S. D. Ha, D. M. Silevitch, and S. Ramanathan, Nat. Phys. **10**, 304 (2014).

[10] A. Subedi, O. E. Peil, and A. Georges, Phys. Rev. B **91**, 075128 (2015).

[11] I. I. Mazin, D. I. Khomskii, R. Lengsdorf, J. A. Alonso, W. G. Marshall, R. M. Ibberson, A. Podlesnyak, M. J. Martínez-Lope, and M. M. Abd-Elmeguid, Phys. Rev. Lett. **98**, 176406 (2007).

[12] P.-H. Xiang, N. Zhong, C.-G. Duan, X. D. Tang, Z. G. Hu, P. X. Yang, Z. Q. Zhu, and J. H. Chu, J. Appl. Phys. **114**, 243713 (2013).

[13] M. Hepting, M. Minola, A. Frano, G. Cristiani, G. Logvenov, E. Schierle, M. Wu, M. Bluschke, E. Weschke, H.-U. Habermeier, E. Benckiser, M. Le Tacon, and B. Keimer, Phys. Rev. Lett. **113**, 227206 (2014).

[14] B. Lau and A. J. Millis, Phys. Rev. Lett. **110**, 126404 (2013).

[15] D. Kumar, K. P. Rajeev, A. K. Kushwaha, and R. C. Budhani, J. Appl. Phys. **108**, 063503 (2010).

[16] M. H. Upton, Y. Choi, H. Park, J. Liu, D. Meyers, J. Chakhalian, S. Middey, J.-W. Kim, and P. J. Ryan, Phys. Rev. Lett. **115**, 036401 (2015).

[17] A. Tiwari, C. Jin, and J. Narayan, Appl. Phys. Lett. **80**, 4039 (2002).

[18] J. Liu, M. Kareev, B. Gray, J. W. Kim, P. Ryan, B. Dabrowski, J. W. Freeland, and J. Chakhalian, Appl. Phys. Lett. **96**, 233110 (2010).

[19] L. M. Rodriguez-Martinez and J. P. Attfield, Phys. Rev. B **58**, 2426 (1998).

[20] A. Berenov, F. Le Goupil, and N. Alford, Sci. Rep. **6**, 28055 (2016).

[21] D. S. Rana, K. R. Mavani, C. M. Thaker, D. G. Kuberkar, D. C. Kundaliya, and S. K. Malik, J. Appl. Phys. **95**, 7097 (2004).

[22] J. P. Attfield, Chem. Mater. **10**, 3239 (1998).

[23] P. V. Vanitha, P. N. Santhosh, R. S. Singh, C. N. R. Rao, and J. P. Attfield, Phys. Rev. B **59**, 13539 (1999).

[24] L. M. Rodriguez-Martinez and J. P. Attfield, Phys. Rev. B **54**, R15622 (1996).

[25] R. J. Goff and J. P. Attfield, Phys. Rev. B **70**, 140404 (2004).

[26] J. P. Attfield, A. L. Kharlanov, and J. A. McAllister, Nature (London) **394**, 157 (1998).

[27] C. P. Tigges, E. L. Venturini, J. F. Kwak, B. Morosin, R. J. Baughman, and D. S. Ginley, Appl. Phys. Lett. **57**, 517 (1990).

[28] J. A. McAllister and J. P. Attfield, Phys. Rev. Lett. **83**, 3289 (1999).

[29] K. Sreedhar, J. M. Honig, M. Darwin, M. McElfresh, P. M. Shand, J. Xu, B. C. Crooker, and J. Spalek, Phys. Rev. B **46**, 6382 (1992).

[30] R. Eguchi, A. Chainani, M. Taguchi, M. Matsunami, Y. Ishida, K. Horiba, Y. Senba, H. Ohashi, and S. Shin, Phys. Rev. B **79**, 115122 (2009).

[31] X. Q. Xu, J. L. Peng, Z. Y. Li, H. L. Ju, and R. L. Greene, Phys. Rev. B **48**, 1112 (1993).

[32] D. Meyers, S. Middey, M. Kareev, M. van Veenendaal, E. J. Moon, B. A. Gray, J. Liu, J. W. Freeland, and J. Chakhalian, Phys. Rev. B **88**, 075116 (2013).

[33] D. Meyers, E. J. Moon, M. Kareev, I. C. Tung, B. A. Gray, J. Liu, M. J. Bedzyk, J. W. Freeland, and J. Chakhalian, J. Phys. D: Appl. Phys. **46**, 385303 (2013).

[34] D. Meyers, S. Middey, M. Kareev, J. Liu, J. W. Kim, P. Shafer, P. J. Ryan, and J. Chakhalian, Phys. Rev. B **92**, 235126 (2015).

[35] G. Catalan, R. M. Bowman, and J. M. Gregg, Phys. Rev. B **62**, 7892 (2000).

[36] K. Hayashi, G. Demazeau, and M. Pouchard, Rev. Chim. Miner. **18**, 148 (1981).

[37] See Supplemental Material at http://link.aps.org/supplemental/10.1103/PhysRevB.96.144411 for XRD comparison of LENO and NNO thin films; the resistivity as a function of temperature of as-grown and O_2-annealed LENO films.

[38] E. Mikheev, A. J. Hauser, B. Himmetoglu, N. E. Moreno, A. Janotti, C. G. Van de Walle, and S. Stemmer, Sci. Adv. **1**, e1500797 (2015).

[39] R. Scherwitzl, P. Zubko, I.G. Lezama, S. Ono, A.F. Morpurgo, G. Catalan, and J.-M. Triscone, Adv. Mater. **22**, 5517 (2010).

[40] L. Wang, S. Ju, L. You, Y. Qi, Y. Guo, P. Ren, Y. Zhou, and J. Wang, Sci. Rep. **5**, 18707 (2015).

[41] J.J. Peng, C. Song, M. Wang, F. Li, B. Cui, G.Y. Wang, P. Yu, and F. Pan, Phys. Rev. B **93**, 235102 (2016).

[42] S. Heo, C. Oh, J. Son, and H. M. Jang, Sci. Rep. **7**, 4681 (2017).

[43] G. Mattoni, P. Zubko, F. Maccherozzi, A. J. H. van der Torren, D. B. Boltje, M. Hadjimichael, N. Manca, S. Catalano, M. Gibert, Y. Liu, J. Aarts, J.-M. Triscone, S. S. Dhesi, and A. D. Caviglia, Nat. Commun. **7**, 13141 (2016).

[44] R. Rana, P. Pandey, S. S. Prabhu, and D. S. Rana, arXiv:1412.3244.

[45] D. S. Rana, J. H. Markna, R. N. Parmar, D. G. Kuberkar, P. Raychaudhuri, J. John, and S. K. Malik, Phys. Rev. B **71**, 212404 (2005).

[46] D. S. Rana, M. Ziese, and S. K. Malik, Phys. Rev. B **74**, 094406 (2006).

[47] R. Rana, P. Pandey, D. S. Rana, K. R. Mavani, I. Kawayama, H. Murakami, and M. Tonouchi, Phys. Rev. B **87**, 224421 (2013).

[48] D. S. Rana, D. G. Kuberkar, and S. K. Malik, Phys. Rev. B. **73**, 064407 (2006).

[49] M. Karttunen, M. Haataja, K. R. Elder, and M. Grant, Phys. Rev. Lett. **83**, 3518 (1999).

[50] R. Mahendiran, A. Maignan, S. Hébert, C. Martin, M. Hervieu, B. Raveau, J. F. Mitchell, and P. Schiffer, Phys. Rev. Lett. **89**, 286602 (2002).

[51] Y. Tokura, Rep. Prog. Phys. **69**, 797 (2006).

[52] P. M. Woodward, T. Vogt, D. E. Cox, A. Arulraj, C. N. R. Rao, P. Karen, and A. K. Cheetham, Chem. Mater. **10**, 3652 (1998).